

OPEN

A novel shockwave-driven nanomotor composite microneedle transdermal delivery system for the localized treatment of osteoporosis: a basic science study

Fan Hu, MD^{a,b,d}, Haojun Liang, MD^{a,b}, Jing Xie, PhD^c, Meng Yuan, PhD^b, Wanxia Huang, PhD^b, Yinze Lei, MD^c, Hao Li, MD^{a,b,d}, Linwen Lv, MD^b, Qiuyang Liu, MD^b, Junhui Zhang, MD^b, Wenxi Su, MD^b, Ranran Chen, MD^b, Zhe Wang, PhD^b, Ya-nan Chang, PhD^b, Juan Li, PhD^b, Cunfeng Wei, PhD^b, Gengyan Xing, PhD^{a,d,*}, Gengmei Xing, PhD^{b,*}, Kui Chen, PhD^{b,*}

Background: Clinical protocols in osteoporosis treatment could not meet the requirement of increasing local bone mineral density. A local delivery system was brought in to fix this dilemma. The high-energy extracorporeal shock wave (ESW) can travel into the deep tissues with little heat loss. Hence, ESW-driven nanoparticles could be used for local treatment of osteoporosis.

Materials and methods: An ESW-actuated nanomotor (NM) sealed into microneedles (MNs) (ESW-NM-MN) was constructed for localized osteoporosis protection. The NM was made of calcium phosphate nanoparticles with a high Young's modulus, which allows it to absorb ESW energy efficiently and convert it into kinetic energy for solid tissue penetration. Zoledronic (ZOL), as an alternative phosphorus source, forms the backbone of the NM (ZOL-NM), leading to bone targeting and ESW-mediated drug release.

Results: After the ZOL-NM is sealed into hyaluronic acid (HA)-made microneedles, the soluble MN tips could break through the stratum corneum, injecting the ZOL-NM into the skin. As soon as the ESW was applied, the ZOL-NM would absorb the ESW energy to move from the outer layer of skin into the deep tissue and be fragmented to release ZOL and Ca²⁺ for anti-osteoclastogenesis and pro-osteogenesis. *In vivo*, the ZOL-NM increases localized bone parameters and reduces fracture risk, indicating its potential value in osteoporotic healing and other biomedical fields.

Conclusion: The ESW-mediated transdermal delivery platform (ESW-NM-MN) could be used as a new strategy to improve local bone mineral density and protect local prone-fracture areas.

Keywords: deep-tissue penetration, extracorporeal shock wave, microneedles, osteoporotic fracture, transdermal drug delivery system

Introduction

The massive bone loss and bone microarchitecture destruction due to osteoporosis may cause osteoporotic fractures, leading to high disability and mortality^[1]. Clinical protocols are mainly administered by intravenous drugs [such as bisphosphonates

(BPs)] to reduce systemic bone loss and lower fracture incidence^[2]. However, systemic administration has a limited protective effect on fracture-prone areas other than the vertebrae, like the femur. Besides, long-term systemic administration may raise the risk of severe side effects, such as atypical femur fractures

^aThe Third Medical Center of Chinese People's Liberation Army General Hospital, ^bKey Laboratory for Biomedical Effects of Nanomaterials and Nanosafety, Institute of High Energy Physics and National Center for Nanosciences and Technology, Chinese Academy of Sciences, ^cState Key Laboratory of Explosion Science and Technology, Beijing Institute of Technology, Beijing and ^dThe Fifth School of Clinical Medicine, Anhui Medical University, Hefei, Anhui Province, People's Republic of China

Fan Hu and Haojun Liang contributed equally to this work.

Sponsorships or competing interests that may be relevant to content are disclosed at the end of this article.

*Corresponding author. Address: Key Laboratory for Biological Effects of Nanomaterials and Nanosafety, Institute of High Energy Physics, Chinese Academy of Sciences, Beijing 100049, People's Republic of China. Tel.: +86 10 88236456. E-mail: chenkui@ihep.ac.cn (K. Chen), and The Third Medical Center of Chinese People's Liberation Army General Hospital, Beijing 100039, People's Republic of China. Tel.: +861 088 236 597; fax: +861 088 236 456. E-mail: xgy1350138@163.com (Gengyan Xing); E-mail: xinggm@ihep.ac.cn (Gengmei Xing).

Copyright © 2024 The Author(s). Published by Wolters Kluwer Health, Inc. This is an open access article distributed under the terms of the Creative Commons Attribution-Non Commercial-No Derivatives License 4.0 (CCBY-NC-ND), where it is permissible to download and share the work provided it is properly cited. The work cannot be changed in any way or used commercially without permission from the journal.

International Journal of Surgery (2024) 110:6243-6256

Received 18 November 2023; Accepted 22 February 2024

Supplemental Digital Content is available for this article. Direct URL citations are provided in the HTML and PDF versions of this article on the journal's website, www.lww.com/international-journal-of-surgery.

Published online 18 March 2024

http://dx.doi.org/10.1097/JS9.0000000000001280

and osteonecrosis of the jaw^[2,3]. Local drug administration may be a vital alternative for preventing osteoporotic fractures^[4].

Microneedles (MNs) could penetrate directly through the stratum corneum and have been used as a minimally invasive and efficient transdermal drug delivery method in tumor and metabolic diseases^[5–8], which is an attractive approach to replace oral delivery of drugs or hypodermic injection to avoid the first-pass effect, reduce the risk of drug side effects, and enhance patient compliance^[9–12]. For instance, researchers reported a bioorthogonal catalytic microneedles patch for cancer therapy capable of producing anti-cancer drugs *in situ*^[8] and archived living cell delivery through cryomicroneedles^[13]. However, the passive diffusion pattern of drug release from microneedles limits drug penetration depth and distribution, so the application of MNs in deep-tissue disease treatment is restricted^[14].

To address the issue, multiple penetration enhancers have been employed to increase drug penetration^[15]. For example, researchers constructed a gas-driven nanomotor (NM) for autonomous and active drug penetration^[16]. However, irregular motions of gas-driven NM reduced the targetability in solid tissue. Exogenous physical stimulation, such as light and magnetic fields, is an alternative driving penetration^[17]. Although these strategies have significantly improved drug penetration, the energy requirements for drug penetration in deep tissues and bone compatibility need to be redefined.

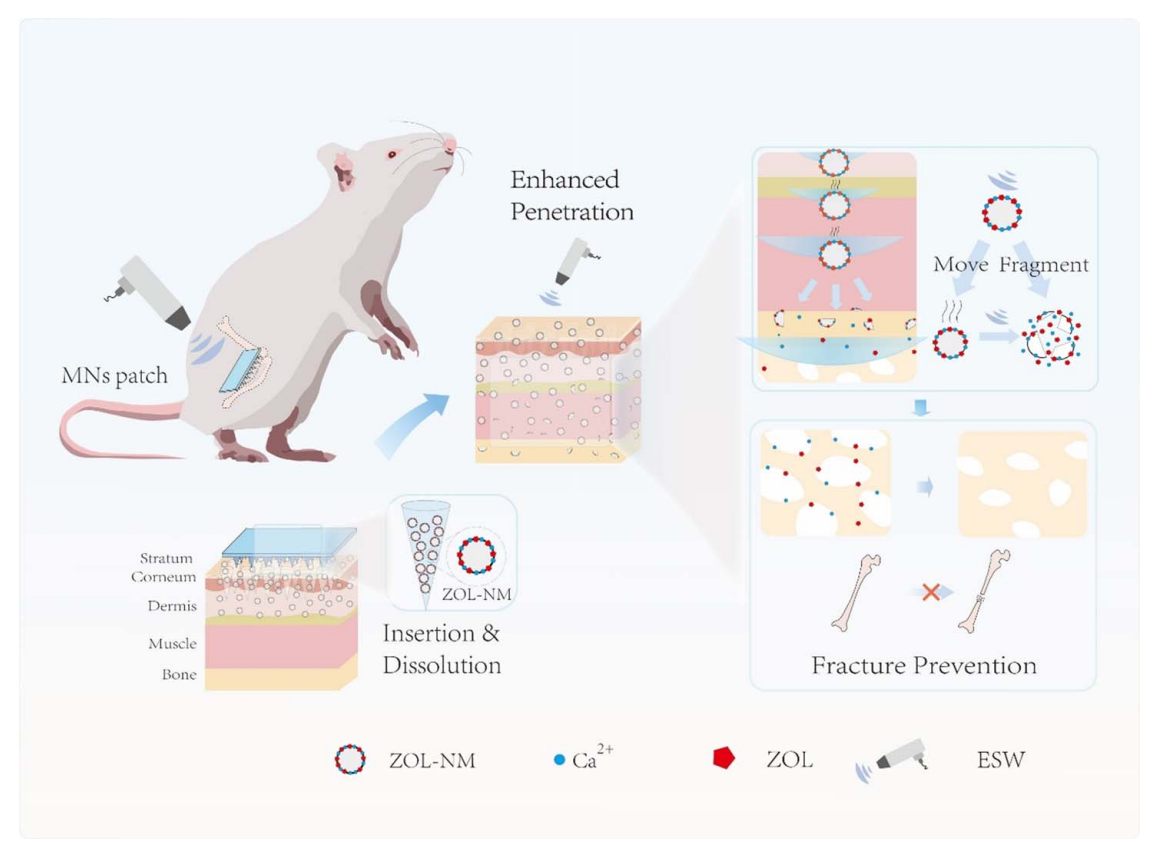
As a high-energy pulse, extracorporeal shockwave (ESW) can travel into the deep tissues with little heat loss^[18]. In our previous studies, ESW is selected as a precisely controlled physical

HIGHLIGHTS

- Based on the strong absorption of extracorporeal shock wave (ESW) by dense matter, we build a novel ESWactuated nanomotor (NM) [zoledronic (ZOL)-NM] for the first time.
- A novel transdermal drug delivery system with outstanding deep-tissue penetration.

stimulation for drug-targeted release^[19,20]. It is worth noting that ESW can generate abundant intensive bubble oscillation and cavitation microstreaming^[21] that can drive the radial motion of nanoparticles through the energy from microbubbles repute generated on the gas–liquid interfaces on the surface of these nanoparticles based on its cavitation effects^[22]. Therefore, ESW may be the driving force in controlling drug penetration in treating deep-tissue diseases, especially bone-related diseases.

As the main component of bone tissue, calcium phosphate (CaP) has good biocompatibility and mechanical conductivity. In our previous works, we selected CaP nanoparticles with high ESW responsiveness in controlled drug release for bone disease^[19,20]. Here, the ESW-NM-MN was designed for osteoporosis protection (Scheme 1). The ZOL-NM with zoledronic (ZOL) as backbone was loaded into MNs and would be released when MNs dissolved after insertion into the skin. Then, the ZOL-NM was propelled by ESW to promote vertical drug penetration in the solid tissue and could also be fragmented by ESW to facilitate the release of ZOL



Scheme 1. The overview of ESW-mediated deep-penetrated ZOL-NM sealed in microneedles for local osteoporosis protection.

and Ca²⁺, resulting in osteoclast inhibition and osteoblast promotion. The local therapeutic effect on osteoporosis (OP) *in vivo* was investigated in an ovariectomy-induced OP rat model. The bone parameters and mechanical properties increased significantly after the ESW-NM-MN treatment.

Experimental section/methods

Materials and reagents

Calcium chloride (CaCl₂), PEG 6000, Tris-Base, Zoledronic Acid (ZOL), and Bovine Serum Albumin (BSA) were purchased from Macklin (Macklin Inc. Shanghai). For cell culturing, α -minimum essential medium (α -MEM; Hyclone Laboratories, Logan, UT, USA), Dulbecco's Modified Eagle's Medium (DMEM; Hyclone Laboratories, Logan, UT, USA), fetal bovine serum (FBS, TransSerum FQ Fetal Bovine Serum, China), streptomycin (10 000 µg/ml; Gibco), penicillin (10 000 U/ml; Gibco) were used. The M-CSF (R&D Systems, Minneapolis, MN, USA) and RANKL (R&D Systems, Minneapolis, MN, USA) were purchased for osteoclast induction. The osteoblast induction medium was purchased from Cyagen, China.

Synthesis of ZOL-NM

ZOL-NM synthesis is based on previous research^[23]. In brief, 0.15 g PEG 6000 was added into 3 ml Tris–HCl (0.5 M, pH = 8), and then the solution was dropped into 2 g Tween 80. The PEG-Tween 80 template was sonicated in an ice water bath for 20 min. Next, 3.55 ml 0.175 M CaCl₂ was added dropwise to the PEG-Tween 80 template and stirred for 30 min, then 10 ml ZOL solution (0.079 g dissolved in 10 ml 0.1 M NaOH) was added dropwise and stirred for 1 h. The reaction system was collected and centrifuged to remove the template.

Synthesis of fluoresce-labeled ZOL-NM

Different fluorescein, including FITC and Cy5, were combined with BSA and loaded into ZOL-NM. In brief, different fluorescein was added into the BSA solution according to the ratio of fluorescein: BSA = 10:1 (M:M). The solution reacted for 2 h at 4°C in the dark, and then excess fluorescein was removed by dialysis. The labeled BSA was obtained by lyophilization of the solution. Labeled BSA weighing 5 mg was added into 3 ml Tris—HCl, and then the steps were followed as described.

To label on calcein, 30 mg calcein was dissolved in 1 ml 0.1 M NaOH, then calcein solution was added into ZOL-NM water decentralized system as calcein: NM=1:10 (V:V). The final product was washed several times with ethanol and water. The labeled ZOL-NM were dispersed in DI (deionized water) water, and fluorescence spectroscopy was scanned using a Microplate Reader (Spark 10M, Tecan).

Characterization of ZOL-NM

The mean nanoparticle size and ζ-potential were measured by Zetasizer Nano (Malvern Panalytical Ltd) at room temperature with a detection angle 90°. ZOL-NM morphology was pictured by a field emission scanning electron microscope (FE-SEM, S-4800, Hitachib) and Transmission Electron Microscope (Tecnai G2 F30). The Infrared Spectrum of ZOL-NM was detected by Micro-FTIR (iN10-IZ10, Thermo) from 400 to

4000 nm⁻¹. The XRD Spectrum (D8 Advance, Bruker) was collected in the range $2\theta = 5-70^{\circ}$, with a 10°/min speed.

The ZOL-NM Affinity to bones

1 mg/ml nanoparticle ethanol suspension was dropped on the surface of the bone and dried at room temperature. Use ethanol to wash the bone surface gently several times and dry at room temperature. Then, the bone surface was observed under SEM.

Finite element model simulation

A linear hardened material model was used to describe the spherical material. The Euler–Lagrange Coupling algorithm (CEL) was chosen to represent the motion process between the spherical particle and the surrounding environment, and the ESW of 2 bar was set for the surface in the contact. The eight-node hexahedral element (C3D8R) was chosen to mesh the nanoparticles, while the EC3D8R was selected as the Eulerian domain element type.

The ZOL-NM motion in gelatin gel

The ZOL-NM suspension was added into a hot 5% gelatin solution. After the hot gelatin solution collided and molded to form a mixed gel, the water-insoluble Oil Red O was minimally injected into the gelatin gel as a marker. The gel was secured to observe a single ZOL-NM in gel under a dark field microscope (Olympus IX73). Then, a 2-bar shockwave was applied to the side of the gel. The position of ZOL-NM was recorded every 500 pulses. The position of ZOL-NM was connected to form the relative displacement curve. The patch length is the sum of distances between two neighboring locations.

Synthesis of nanoparticle-loaded microneedles

In brief, a 0.5 ml 1 mg/ml nanoparticle dispersion system (in DI water) was poured into the microneedles polydimethylsiloxane mold. Then, the mold was placed in the vacuum and evaluated to – 30 mmHg for 20 min. Remove the excess solution and add 0.6 ml 20% (wt%) hyaluronic acid. Dry the samples at 40°C overnight. Take the microneedles carefully and store them at room temperature.

Mechanical test

The mechanical strength of microneedles was tested using an Instron 5985 tensile meter. In brief, MNs were placed horizontally on the test plate with the tips upon them. A cylindrical probe slowly descended vertically towards MN tips at 0.5 mm/s. Collect data and plot force–displacement curves. The blank MNs and nanoparticles loaded MNs were tested for comparison.

Primary cell isolation

A 4-week-old female C57BL/6N mouse was decollated and sterilized by immersion in 75% alcohol for 5 min. Femurs were completely and carefully isolated from the body. The primary bone marrow cells were flushed out from the bone marrow cavity and resuspended in a culture flask using $\alpha\text{-MEM}$. After culturing for 24 h, the suspended cells in the culture medium were collected and removed to two new culture flasks cultured with $\alpha\text{-MEM}$ (maintain 30 ng/ml M-CSF) for bone marrow monocyte (BMM), and the adherent cells were cultured with DMEM for bone marrow stem cells (BMSC) $^{[24]}$.

Cell viability assay

The BMM and BMSC cells were placed in 96-well plates, with 5×10^3 cells per well, and left to culture for 2 days. After that, the old medium was replaced with a fresh medium that contained either 0, 0.5, 1, 2, 5, or 10 μ M/ml of ZOL or ZOL-NM (ZOL was used as a normalized standard). The cells were then left to culture for an additional 24 or 48 h, after which the CCK-8 solution was added. Following the instructions of the reagent, the optical density (OD) value was detected at 450 nm.

Osteoclast culture

The cultivation of osteoblasts was based on our previous work $^{[25-28]}$. After culturing BMM cells for 3 days, we planted them into 96-well plates with $\alpha\text{-MEM}$, which maintained 30 ng/ml M-CSF and 50 ng/ml RANKL. The mediums also contain different ingredients (1 $\mu\text{M/ml}$ ZOL, 1 $\mu\text{M/ml}$ ZOL-NM, 1 $\mu\text{M/ml}$ ZOL-NM+2 bar ESW). Incubate cells for 4 days, observe under the microscope, and stain with a TRAP staining kit following instructions.

Osteoblast culture

The BMSC was planted into 24-well plates with DMEM for 3 days. Then, the Osteoblast induction medium was added to incubate the osteoblast. The mediums contain different ingredients (1 μ M/ml ZOL, 1 μ M/ml ZOL-NM, 1 μ M/ml ZOL-NM+2 bar ESW). After incubating for 2 weeks, observe cells under the microscope and stain with an Alizarin Red Stain Kit. The cells were placed in 10% cetylpyridinium chloride monohydrate for statistical analysis at 562 nm.

Enhanced biodistribution of ZOL-NM in vivo

The In Vivo Imaging System (IVIS) was used to show the biodistribution of ZOL-NM *in vivo*. Briefly, three 8-week-old SD (Sprague–Dawley) rats were divided into control and ESW-NM-MN groups, and the hair around the lower limbs was removed. The different fluorescein (Calcein and Cy5) labeled ZOL-NM were loaded into MNs. Then, the MNs were administrated on the left limbs for 30 min. 2 bar ESW was applied on the area of MNs administration 2000 times in the ESW-NM-MN group. The rats were sacrificed at different points in time to peel the femurs and count the mean fluorescence intensity of the femurs.

Synchrotron radiation proportional computed tomography and slices section for porcine skin

The fresh porcine skin was collected from the supermarket, and the hair was removed. Rinse several times with water and cut the skin into 1.5×1.5 cm size pieces. Then, the microneedles loaded with ZOL-NM were inserted into the pieces for 30 min. Parts of the pieces received 2 bar ESW as the experimental group. Then, the skin samples were fixed with 4% paraformaldehyde. For Synchrotron Radiation Proportional computed tomography (CT) scanning, the ZOL-NM was doped with Cu by adding CuO into the Tween 80 and PEG temple as described – gradients dehydration of the sample with different concentrations of ethanol solution. A 5×5 mm-sized block of skin was excavated in the microneedle application area to scan with a resolution of 2.3 μ m. The images and statistic results were processed by Avizo 2019.1. For the slices section, the ZOL-NM was labeled with

FITC as described. Gradient dehydration with different concentrations of sucrose solution. The skin was embedded by OCT (optimal cutting temperature compound) and cut into 15 μ m sections by frozen section. The fluorescence was observed under a confocal microscope.

Ovariectomized rat mold and treatment

Based on the 3R (reduction, refinement, and replacement) principle, we have reduced the number of animals while remaining statistically valid. The ovariectomized model was built in our previous work^[27]. Briefly, thirty-six 8-week-old SPF-grade female SD rats (purchased from Vital River, Beijing) were included in the experiment, and those weighing more than 250 g or less than 160 g were excluded. The rats' ovaries were ligated through a dorsal opening after they were given anesthesia. The SHAM group did not remove the ovaries after opening the abdominal cavity through the dorsal opening. After surgery, the rats were kept in an animal room equipped with IVC at 25°C for 6 weeks to develop osteoporosis.

Ovariectomized rats were divided into six groups of six rats each by simple randomization

OVX group, ZOL (i.v.) group, ZOL-NM-MN group, ESW group, and ESW-NM-MN group (n=6). Remove the left hind limb hair of rats under anesthesia before treatments. The ZOL (i.v.) groups were given a single injection of 200 µl zoledronic PBS solution (200 µg/ml) through the tail vein. The ZOL-NM loaded microneedles were applied near the femur on the left limbs of the MN and ESW-NM-MN groups for 30 min. Then, the ESW-NM-ZOL-NM-MN group applied ESW (2 bar, 8 Hz, and 2000 pulses) at the microneedle application area for once. The ESW group applied ESW (2 bar, 8 Hz, and 2000 pulses) at the same area for once. After 6 weeks of treatment, the rats were executed. The femurs and spines were excised and cleared of fat and connective tissues. The skin of MNs and ESW application was collected, too.

Micro-CT evaluation and histological staining

All rats were sacrificed after treatment for 6 weeks. The femurs of rats were stripped to analyze the anti-osteoporosis effects of microneedles. Micro-CT was performed to scan the distal femurs of each group at a resolution of 13 μ m. The images were processed by Avizo 2019.1. Selected 100 slices on the epiphysis were rebuilt in 3D to calculate related bone parameters, including bone volume fraction (BV/TV), Trabecular thickness (Tb. Th), trabecular Separation (Tb. Sp), bone surface area to tissue volume ratio (BS/TV). Major organs (including heart, liver, spleen, lung, and kidney) and decalcified bone were cut into 10 μ m sections and stained for hematoxylin and eosin (H&E) or TRAP staining and BMP-2 immunohistochemical staining (n = 3).

Three-point bending test

The bones were stripped and fixed in 4% paraformaldehyde. The three-point bending test was performed on the electronic universal testing machine (CMT6103). Before testing, the bone (n=3) was washed with phosphate-buffered saline (PBS), and residual muscles on the surface of the diaphysis were removed. Then, bones were placed at a bracket that fixed the ends of the bone in place while a measured amount of force was applied perpendicular to the midpoint of the anterior side of the

diaphysis. Force was applied at the 4 mm/min rate until the bone fraction. The elasticity of bone was calculated as^[29,30].

$$E = \frac{FL}{48DI}, I = \frac{\pi}{4}(a'b'^3 - ab^3)$$

The D is the max displacement of bone, and F is the corresponding force during the elastic deformation. The L is the distance between them, which is the distance between the fulcrums of the bracket. The a', b', and a, b are the outer and inside diameters of bone. Repeat three times for each group.

Analysis of ZOL-NM distribution in plasma

To analyze the biodistribution in plasma, the blood of SD rats was collected by a retro-orbital puncture at various time points from 30 min after labeled ZOL-NM loaded microneedle application. Plasma was isolated by centrifugation at 1500g for 10 min. Then, 30 μ Llplasma was diluted into 90 μ l with PBS to scan fluorescence spectra.

Statistics analysis

Data were processed using IBM SPSS statistics software (Chicago, USA). All the present data were calculated as mean \pm standard deviation (SD). Data were reported as biological replicates in at least three independent experiments. Differences among groups were assessed using the analysis of variance (ANOVA) or Students' t tests. P < 0.05 was considered statistically significant. Animal experiments were conducted in a double-blind manner, and the grouping and results were not known to the observer until after data recording was completed.

Results

Characterization of ZOL-NM

Self-propelled NMs are overly focused on fuel-driven and chemotactic behavior, generally composed of at least two units to archive directional motion^[31,32]. In targeted therapeutics, external stimuli are often more advantageous considering biomedical applications^[33]. ESW with high energy can be used as a driving force for NM.

Materials respond differently to the ESW due to Young's modulus^[27]. Calcium phosphate (CaP) material with a high Young's modulus has good bone compatibility and has been used to construct ESW-responsible drug-releasing nanoparticles in our previous works. A finite element model of the nanoparticles in the tissue environment was established to investigate the stiff CaP nanoparticles' motion in solid tissue under ESW. The properties of the CaP material used in the simulation were tested in our previous work (Young's modulus = 26.6 GPa)^[19], and the ESW of 2 bars was set on the nanoparticles. The simulation result showed that the kinetic energy of the CaP nanoparticles increased dramatically compared with the soft tissue under a single pulse of ESW (Fig. 1A), showing the excellent ESW absorbing ability of the CaP nanoparticles. Meanwhile, the displacement of nanoparticles was also observed (Fig. 1B), which demonstrated that the stiff CaP could be selected as the substrate to construct the NM with directional motion ability.

Hence, we built stiff nanoparticles (ZOL-NM) with high responsiveness to ESW for deep penetration. The ZOL-NM was

synthesized by template method. The PEG and Tween 80 were used to form the temple (Supplementary Fig. S1, Supplemental Digital Content 1, http://links.lww.com/JS9/C143), and the CaCl₂ and ZOL were used as the calcium and phosphorus sources, respectively, to form the stiff shell. The hydrodynamic particle size and zeta potential were 179.27 ± 9.67 nm and -19.5 ± 0.89 mV (Fig. 1C). The transmission electron microscope (TEM) results showed the spherical structure at the size of 66.12 ± 18.68 nm (Fig. 1D) and a homogeneous solid structure of ZOL-NM (Fig. 1E). To investigate the stability of ZOL-NM, FITC-labeled BSA was sealed into ZOL-NM. After dispersing in PBS for 4 days, the fluorescence intensity of the supernatant was measured, and it was found to be little changed, indicating the good stability of ZOL-NM (Supplementary Fig. S2, Supplemental Digital Content 1, http://links.lww.com/JS9/C143; Supplementary Fig. S3, Supplemental Digital Content 1, http://links.lww.com/JS9/C143; and Supplementary Fig. S4, Supplemental Digital Content 1, http://links.lww.com/JS9/C143).

We investigated the component of ZOL-NM as well. The Fourier Transform Infrared (FTIR) spectra showed peaks at 1095 and 1550 cm $^{-1}$ in ZOL-NM, which coincided with the P–O of ZOL and the C=C of imidazole ring, respectively (Fig. 1F). Besides, the ultraviolet-visible (UV-Vis) absorption peak at 210 nm also described the presence of ZOL in nanoparticles (Fig. 1G). The UV-Vis also showed that the load rate of ZOL in ZOL-NM reached 75.0 \pm 0.6%. The amorphous calcium phosphate structure of ZOL-NM was confirmed by X-ray powder diffraction (XRD) with a single peak around 30° (Supplementary Fig. S5, Supplemental Digital Content 1, http://links.lww.com/JS9/C143).

To observe the ZOL-NM motion upon the ESW application, we mixed the ZOL-NM into gelatin to make a gel. The motion trajectories and relative displacement of ZOL-NM upon ESW were recorded under a dark field microscope (Fig. 1H). With some random motion on the way, the ZOL-NM moved with the direction of ESW overall (Fig. 1I). We also tested the corresponding displacement and chemotactic index (the ratio of total displacement to path length) to estimate the migration persistence (Fig. 1J). The results showed that the ZOL-NM had an average displacement at $2.68 \pm 0.58 \,\mu m$ per 500 pulses and a chemotactic index of 0.23 under ESW. All these results demonstrated that the ZOL-NM could follow the direction of ESW.

ESW-NM-MN penetrated through solid tissue and accumulated in the bone locally

To investigate the orienteering of the ZOL-NM in the solid tissue upon the ESW application, the ZOL-NM loaded MNs were first fabricated (Fig. 2A). The increased failure force of ZOL-NM loaded MNs, from 3.2 N of blank MNs to 4.5 N, indicated a better mechanical strength to break through the tissue barrier (Fig. 2B). Fluorescence imaging demonstrated the successful loading of ZOL-NM in microneedle tips rather than the substrate (Fig. 2C).

Then, the ZOL-NM loaded MNs were applied on the porcine skin for 30 min *in vitro*. The ZOL-NM was labeled with FITC for depth measurement. The average penetration depth of ZOL-NM showed a significant increase under the ESW application, which reached 1221.63±98.80 μm, while the average depth was only 687.53±181.27 μm without ESW (Fig. 2D, E). To visualize the distribution of ZOL-NM in the

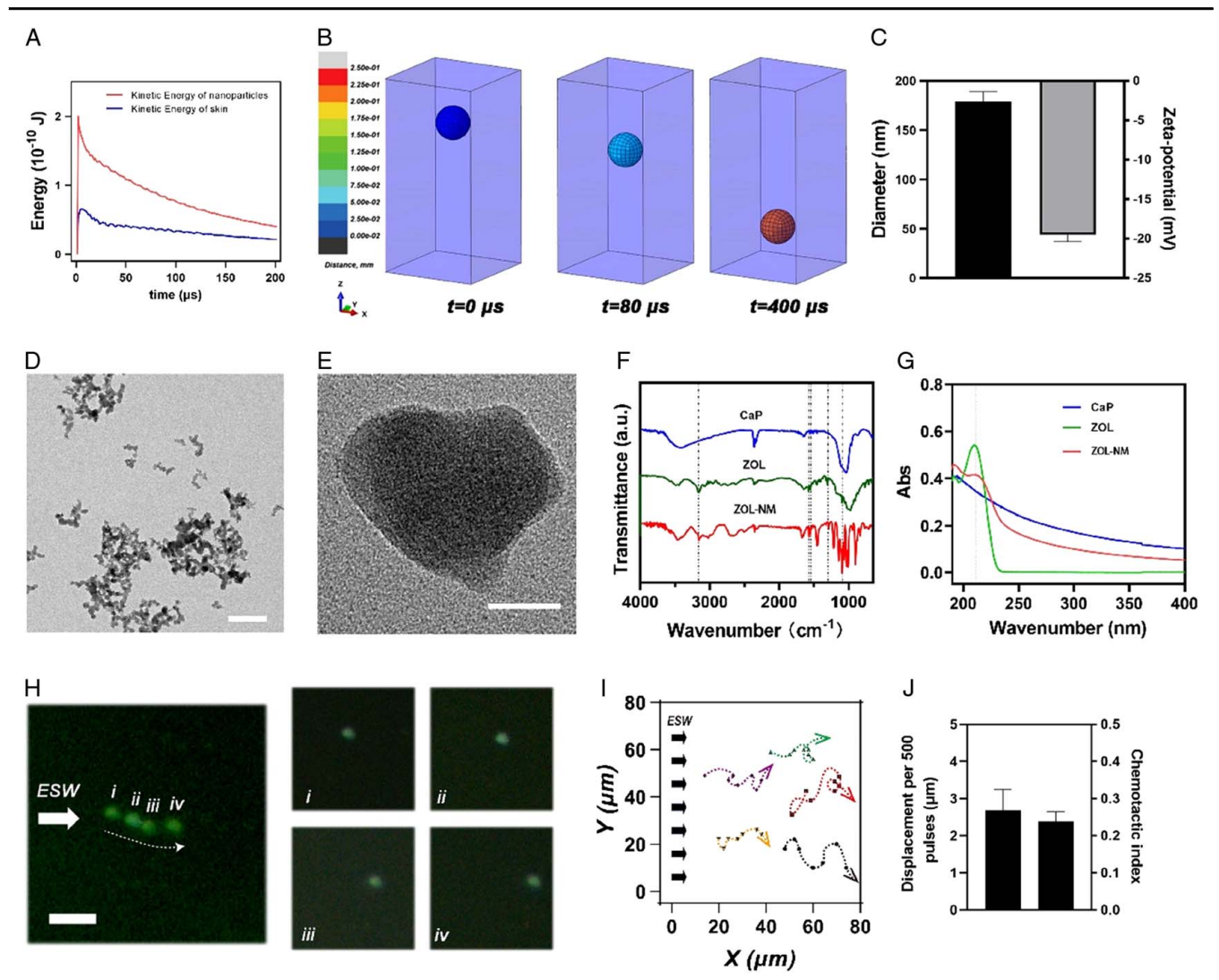


Figure 1. The synthesis and characterization of ZOL-NM. (A) Finite element analysis simulating the kinetic energy of nanoparticles and skin under a single shock wave. (B) The simulation of ZOL-NM's movement under ESW. (C) The hydrodynamic size and zeta potential of ZOL-NM. (D) TEM of ZOL-NM. Scale bar = 500 nm. (E) The enlarged image of the single ZOL-NM. Scale bar = 50 nm. (F) FTIR of CaP, ZOL, and ZOL-NM. (G) The UV absorption spectroscopy of ZOL-NM. (H) The motion trajectories of one ZOL-NM with ESW under a dark field microscope. The white arrow represents the direction of ESW. Scale bar: 10 μ m. (i)—(iv): The relative position of one nanomotor under the 0, 1000, 1500, and 3000 ESW application times. (I) the relative motion of ZOL-NM with ESW. The colored dotted line represents the simulated motion route of ZOL-NM and the black arrow for the direction off ESW. (J) The displacement per 500 pulses shockwave and chemotactic index (ratio of distance to path length) of ZOL-NM.

skin, the synchrotron radiation proportional CT was performed by introducing Cu into the ZOL-NM to increase the contrast^[34]. Segmentation by the threshold, the 3D reconstruction results showed that the ZOL-NM was distributed in the whole layer of the skin after MN application (Fig. 2F and Movie S1, Supplemental Digital Content 2, http://links.lww. com/JS9/C144; Supplemental Digital Content 1, http://links. lww.com/JS9/C143; S2, Supplemental Digital Content 3, http://links.lww.com/JS9/C145; Supplemental Digital Content 1, http://links.lww.com/JS9/C143; Supporting Information, Fig. S16, Supplemental Digital Content 1, http://links.lww. com/JS9/C143). We divided the skin evenly into two layers of ~1 mm thickness on the upper and lower to compare the penetrance and distribution of particles by calculating the total volume of accumulated ZOL-NM. Conspicuously, the volume ratio of ZOL-NM in the skin's lower and upper layers

increased significantly from 50 to 150% under ESW, indicating the actuated motion of ZOL-NM in solid tissue by ESW (Fig. 2G).

Furthermore, the enhanced enrichment to the skeleton of ZOL-NM by ESW was also verified. The ZOL-NM showed a high bone affinity and bone targeting *in vivo* (Supplementary Fig. S6, Supplemental Digital Content 1, http://links.lww.com/JS9/C143). Next, the ZOL-NM dual labeled by Calcein and Cy5 was loaded into microneedles (Supplementary Fig. S7, Supplemental Digital Content 1, http://links.lww.com/JS9/C143) and applied to rats. The IVIS results showed that the mean fluorescence intensity of both Calcein and Cy5 of the ESW-treated femur was increased by about 20% compared with that of the non-treated side, indicating the local enhancement targeting effect of ZOL-NM under the ESW-NM-MN application (Fig. 2H, I).

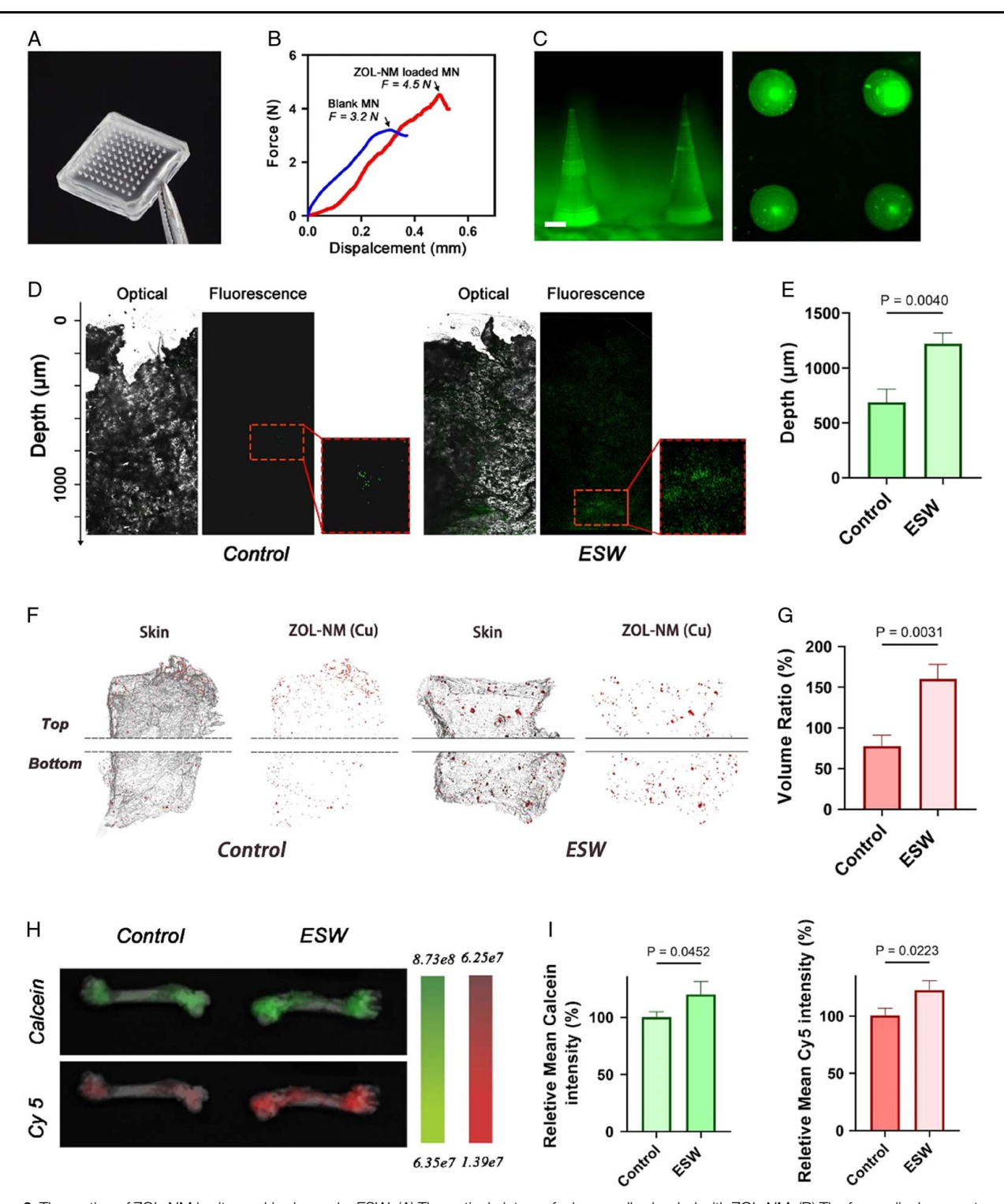


Figure 2. The motion of ZOL-NM in vitro and in vivo under ESW. (A) The optical picture of microneedles loaded with ZOL-NM. (B) The force—displacement curve of microneedles. Red line: ZOL-NM loaded MNs; blue line: blank MNs. (C) The fluorescence imaging of microneedles. Scale bar: 200 µm. (D, E) The optical and fluorescence image of skin after MN administration. (F) Synchrotron radiation proportional CT of ZOL-NM in the skin. (G) The volume ratio of ZOL-NM in the lower and upper layers of the skin. (H, I) The femur's IVIS imaging and relative mean fluorescence intensity after MN administration.

ESW-NM-MN inhibited osteoclastogenesis and promoted osteogenesis

The ZOL inhibits bone resorption due to the inhibition of osteoblast activity. To investigate the ZOL release from ZOL-

NM, we measured the fragmenting efficiency of ZOL-NM under ESW by detecting leaked FITC after fragmenting labeled ZOL-NM by ESW. The results showed that the application of ESW resulted in the leakage of green fluorescence from ZOL-NM. It

was almost wholly leaked out after ESW was applied about 7000 times (Fig. 3A). Using an inductively coupled plasma optical emission spectrometer (ICP-OES), we detected the incremental release of ZOL and Ca²⁺ from treated ZOL-NM (Fig. 3B), which confirmed the release of ZOL and Ca²⁺ from the fragmentation of ZOL-NM by ESW.

Then, we detect cytotoxicity on bone marrow macrophages (BMM) and bone marrow mesenchymal stem cells (BMSC) of ZOL-NM. The concentration of ZOL-NM was normalized by the amount of ZOL. As shown in Figure 3C, after 24 and 48 h of cocultivation with different concentrations of ZOL-NM, the ZOL-NM did not show apparent cytotoxicity on the two kinds of cells compared with ZOL. The Cell Live/Death staining also confirmed the results (Supplementary Fig. S8, Supplemental Digital Content 1, http://links.lww.com/JS9/C143; Supplementary S9, Supplemental Digital Content 1, http://links.lww.com/JS9/C143). Then, we added 1 μ M ZOL, 1 μ M ZOL-NM, and 1 μ M ZOL-NM fragmented by ESW into the culture system to observe the anti-osteoclast effects of ZOL-NM by TRAP

staining. After incubating for 2 days, all treatments reduced osteoclast maturation significantly compared to the control groups (Fig. 3D). Compared with the control group (46.11%), the TRAP-positive area decreased significantly to 6.17% in the ZOL group, 5.57% in ZOL-NM group, and 4.44% in ZOL-NM + ESW group and there was no significant difference between different treatments, which showed the equal anti-osteoclastogenesis effects of ZOL-NM to ZOL alone (Fig. 3E). We next verified the pro-osteogenesis of ZOL-NM. The Alizarin Red S was applied to stain the calcium nodules as the marker of osteoblast differentiation maturation. The stained calcium nodules were more numerous and larger in the ZOL-NM and ESW + ZOL-NM groups (Fig. 3F). To quantify the mineralization degree, Alizarin red S was further extracted using 10% cetylpyridinium chloride monohydrate, and the OD of the solution at 562 nm was measured (Fig. 3G). The better-increased mineralization degree was observed in the ESW + ZOL-NM treatment, which suggested the pro-osteogenesis effects of ESW + ZOL-NM.

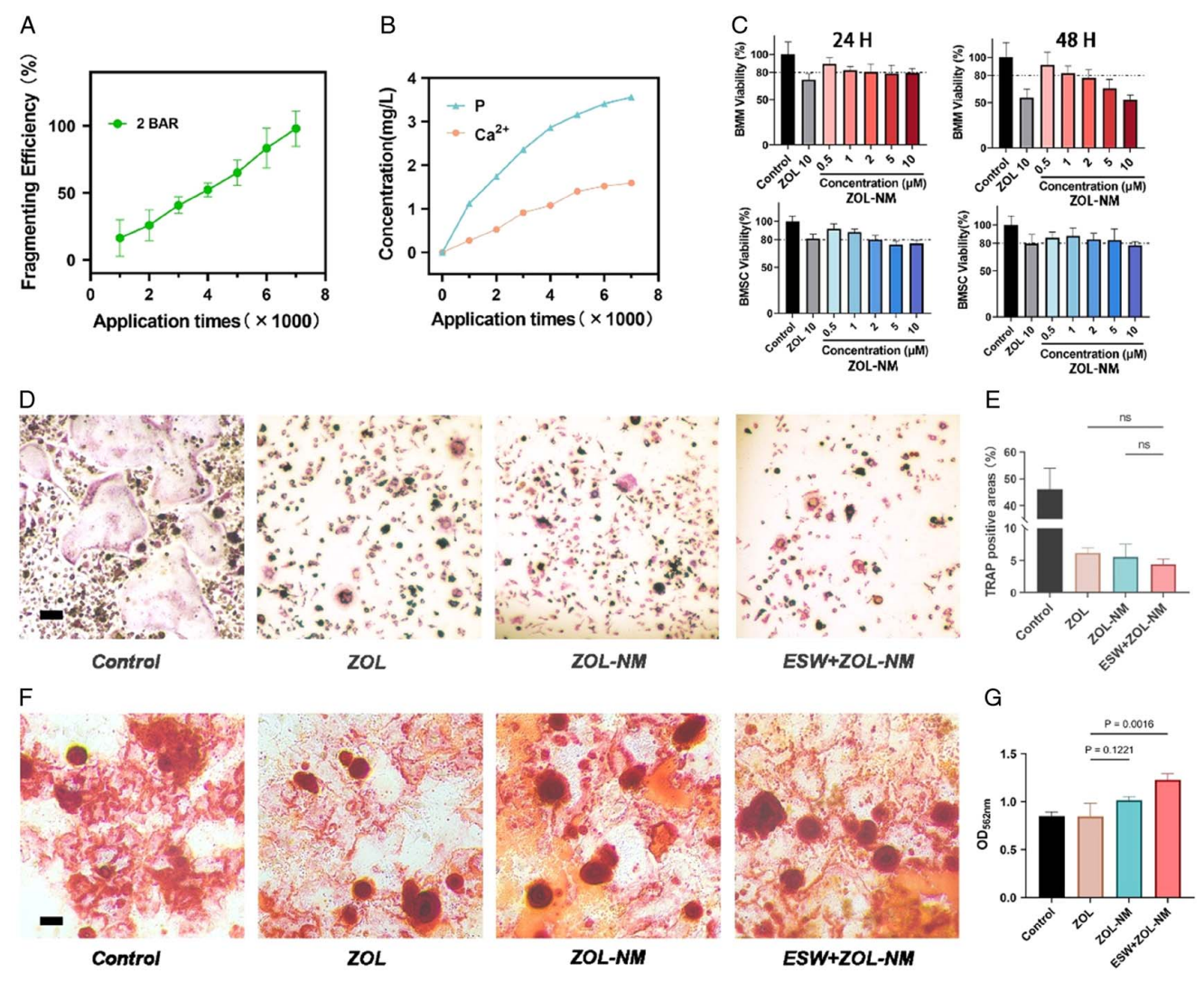


Figure 3. The anti-osteoclast and pro-osteoblast effects of ZOL-NM. (A, B) The fragmenting efficiency of ZOL-NM and the drug release under ESW. (C) The cell viability of BMM and BMSC. Red: BMMs; blue: BMSCs. (D) the TRAP staining of osteoclast after different treatments. Scale bar = 100 μm. (E) The quantified result of TRAP-positive areas. (F) The Alizarin Red S staining of osteoblast after different treatments and (G) the quantified result of Alizarin Red S staining.

Localized therapy effect of ESW-NM-MN in vivo

To verify the localized therapeutic effect of ESW-NM-MN delivery system, the OVX rat model was established and divided into different groups of six rats each. Six weeks after surgery, the microneedles were administered on the left femur for 30 min, and then ESW (2 bar, 2000 shocks) was applied. The rats were sacrificed, and both sides of the femurs were collected for micro-CT scanning and histochemistry analysis in week 12 (Fig. 4A).

The micro-CT reconstruction showed that the bone volume of the left femur (the treated side of the ESW-NM-MN group) increased significantly in the ESW-NM-MN group, compared with other treatments (Fig. 4B, Supplementary Fig. S10, Supplemental Digital Content 1, http://links.lww.com/JS9/C143; Fig. S11, Supplemental Digital Content 1, http://links.lww.com/JS9/C143). Notably, the left femur showed better micro-architecture and a higher bone mass than the right femur. The bone parameters, including bone volume per tissue volume (BV/TV), bone surface per tissue volume (BS/TV), the trabecular thickness (Tb. Th), the trabecular separation (Tb. Sp), and trabecular number (Tb. N) of the left femur also showed a significant improvement compared to the contralateral side (Fig. 4C).

The TRAP and BMP-2 IHC staining were executed to evaluate the bone resorption and formation activity, respectively. The results showed that the TRAP-positive cells were mostly reduced in the ESW-NM-MN group's left femurs (Fig. 5A, B). The upregulation of BMP-2 expression was available as well (Fig. 5C), and the highest BMP-2 was observed in the left femur in the ESW-NM-MN groups, suggesting the most elevated localized anabolic metabolism with the treatment of ESW-NM-MN (Fig. 5D).

The bone's macro-mechanical effects were examined via a three-point bending test to evaluate the fracture resistance. The maximum load force of the left femur rose to a higher level (145.51±9.49 N) in the ESW-NM-MN group compared with other treatment groups (115.87±10.03 N for the ESW group and 127.37±14.31 N for the ZOL-NM-MN group) (Fig. 5E, Supplementary Fig. S12, Supplemental Digital Content 1, http://links.lww.com/JS9/C143). The average Young's modulus of left femurs also improved by 33% compared with the contralateral sides in the treatment of the ESW-NM-MN group, showing the best fracture resistance in various treatment outcomes (Fig. 5F).

Systemic anti-osteoporosis effects of ESW-NM-MN

It is necessary for systemic treatment to reduce systemic bone loss at the same time^[35]. The intravenous injection of zoledronic [ZOL (i.v.)] was contrasted to evaluate the systemic anti-osteoporosis effect of ESW-NM-MN (Fig. 6A). The right femurs and L3 vertebrae, non-treated side, were selected to verify the systemic effects. The micro-CT reconstruction results showed a noticeable improvement in trabecular structure in both ESW-NM-MN and ZOL (i.v.) groups, with no apparent differences (Fig. 6B, C). Furthermore, the bone resorption and formation activity assessed by TRAP and BMP-2 IHC staining showed no apparent differences between them as well (Fig. 6D-G). The biomechanics testing results could not differentiate between the fracture resistance ability of each treatment (Fig. 6H, I, Supplementary Fig. S13, Supplemental Digital Content 1, http:// links.lww.com/JS9/C143). In addition, the evaluation of the vertebrae showed no significant differences between ZOL (i.v.) and ESW-NM-MN group (Fig. 6J, K, Supplementary Fig. S14, Supplemental Digital Content 1, http://links.lww.com/JS9/ C143), indicating the systematical anti-OP effect of ESW-NM-MN. The systemic anti-OP effect may contribute to that part of released ZOL-NM from MNs entering the blood circulation through the subdermal capillary network and distributing systemically (Supplementary Fig. S15, Supplemental Digital Content 1, http://links.lww.com/JS9/C143).

Discussion

In this study, we established an ESW-driven NM (ZOL-NM) for local protective effect through microneedles administration. We prepared NMs using ZOL as the backbone, which could absorb the energy of ESW and direct movement, thereby achieving deeptissue penetration. Besides, the NM would be fragmented by ESW to release ZOL and Ca²⁺ to archive anti-osteoclast and proosteoblast effects. We verified the therapeutic effects of the NM on the OVX rat model, which showed better bone parameters and mechanical structure. It is worth mentioning that NMs can also exert a systemic therapeutic effect similar to intravenous administration of ZOL.

Osteoporosis is closely related to the imbalance of bone formation and bone resorption. Clinical drugs to treat osteoporosis mainly include drugs that promote bone formation and bone resorption inhibitors. Drugs that promote osteogenesis stimulate osteoblast differentiation and bone mineralization, promoting bone formation and increasing bone strength [36,37]. For instance, teriparatide, a recombinant human parathyroid hormone analog (PTH), plays an important role in the osteoblast antiapoptotic effect through PTH1R^[38]. Besides, teriparatide stimulates the release of growth factors, which enhances the migration and differentiation of osteoblasts, promoting osteogenesis. In addition, some calcium supplements and vitamins can also have similar effects. Bone resorption inhibitors, including selective estrogen receptor modulators (SERMs)[39], calcitonin[40], and bisphosphonates (BPs)[41], are used more often clinically to treat osteoporosis. SERMs are not estrogens but can recognize and bind to estrogen receptors (ER) in bone tissue, thus exerting estrogen-like effects, like inhibiting bone resorption, increasing bone density, and reducing the risk of vertebral and nonvertebral fractures^[42]. Calcitonin is a peptide hormone secreted by the parafollicular cells of the thyroid gland, which could reduce blood calcium and phosphorus levels. Calcitonin could inhibit osteoclast motility by modulating cAMP, RANK/RANKL, Src, and tyrosine kinase Pyk2 and inhibit bone resorption^[43]. Furthermore, it may trigger bone formation by increasing Wnt10b expression in osteoclasts, leading to mineralization via the Wnt/β-catenin pathway^[44].

BPs are currently the first choice for the treatment of osteoporosis, including ZOL. ZOL can tightly bind to the surface of hydroxyapatite, thereby interfering with osteoclast attachment. Meanwhile, ZOL can induce NADPH oxidase-mediated ROS production, leading to PI3K/AKT inactivation, glycogen synthase kinase (GSK)-3β activation, and myeloid cell leukemia 1 (Mcl-1) downregulation, thereby further inducing pre-osteoclast cell apoptosis [45]. After intravenous injection, ZOL is mainly combined with bone tissue in the body, and the remaining drug in the blood will be excreted through the kidneys. The blood drug concentration is less than 1% of the peak after 24 h [46]. The ZOL combined with bone tissue will slowly release into the tissues and maintain a deficient concentration in the blood. Long-term

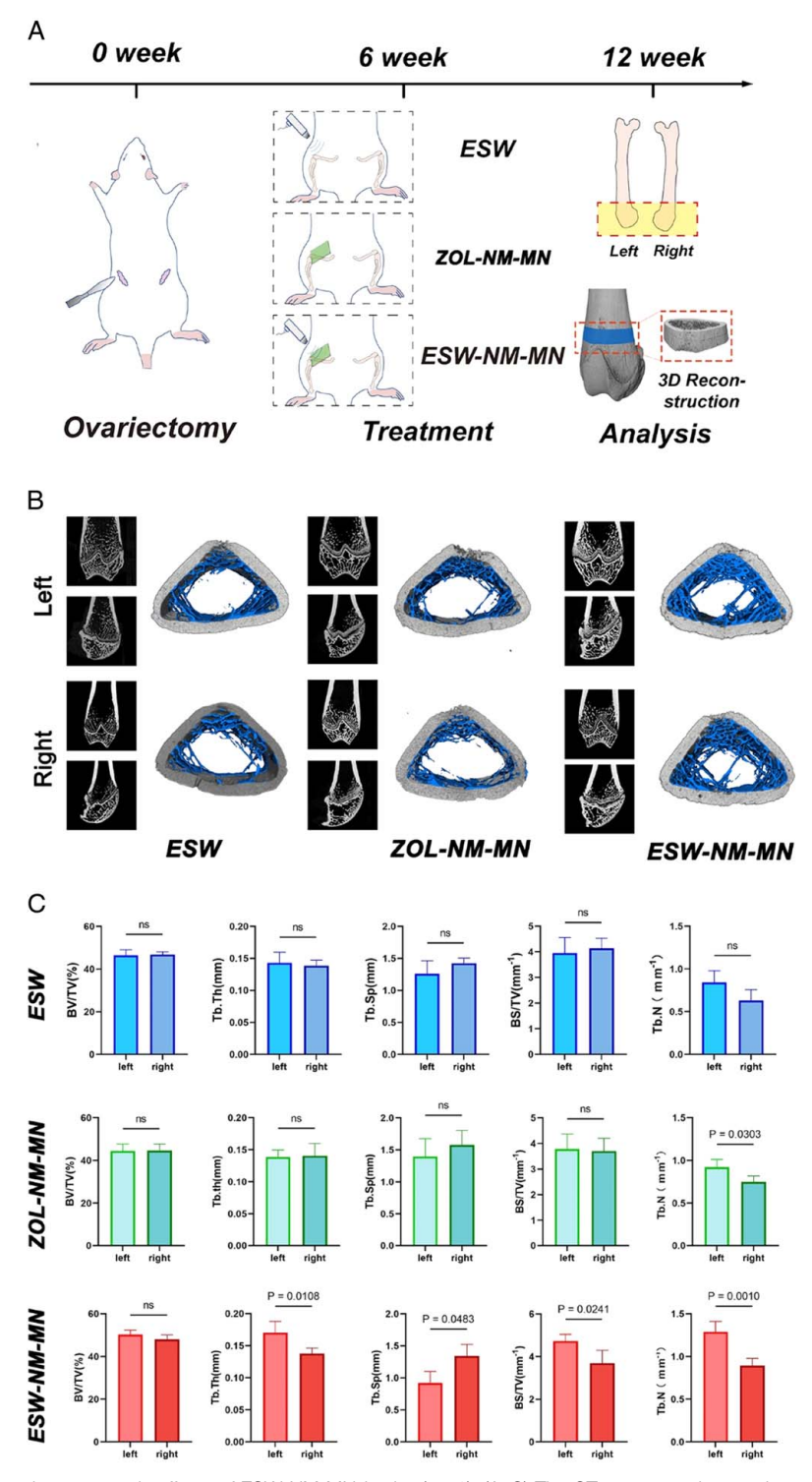


Figure 4. The local enhanced anti-osteoporosis effects of ESW-NM-MN $in \ vivo \ (n=6)$. (A–C) The CT reconstruction results and statistical analysis of different treatment groups. The blue area in (B): the cancellous bone and the gray area in (B): cortical bone.

intravenous infusion of ZOL can cause various adverse reactions (such as gastroesophageal irritation, renal toxicity, osteonecrosis of the jaw (ONJ), atypical fractures, etc.), reducing the quality of life of elderly patients^[47]. Therefore, it is still necessary to find new ways of administration to reduce drug dosage and reduce the chance of side effects. In this study, we prepared calcium

phosphate NM with ZOL as the backbone, namely ZOL-NM. We examined the release of drugs after applying ESW, and the results showed that ESW can serve as a 'switch' to control drug release (Fig. 3A, B). Experiments on drug concentration in the blood also showed that we delayed the peak blood concentration of the ZOL-NM by 2 h through MN administration, comparing

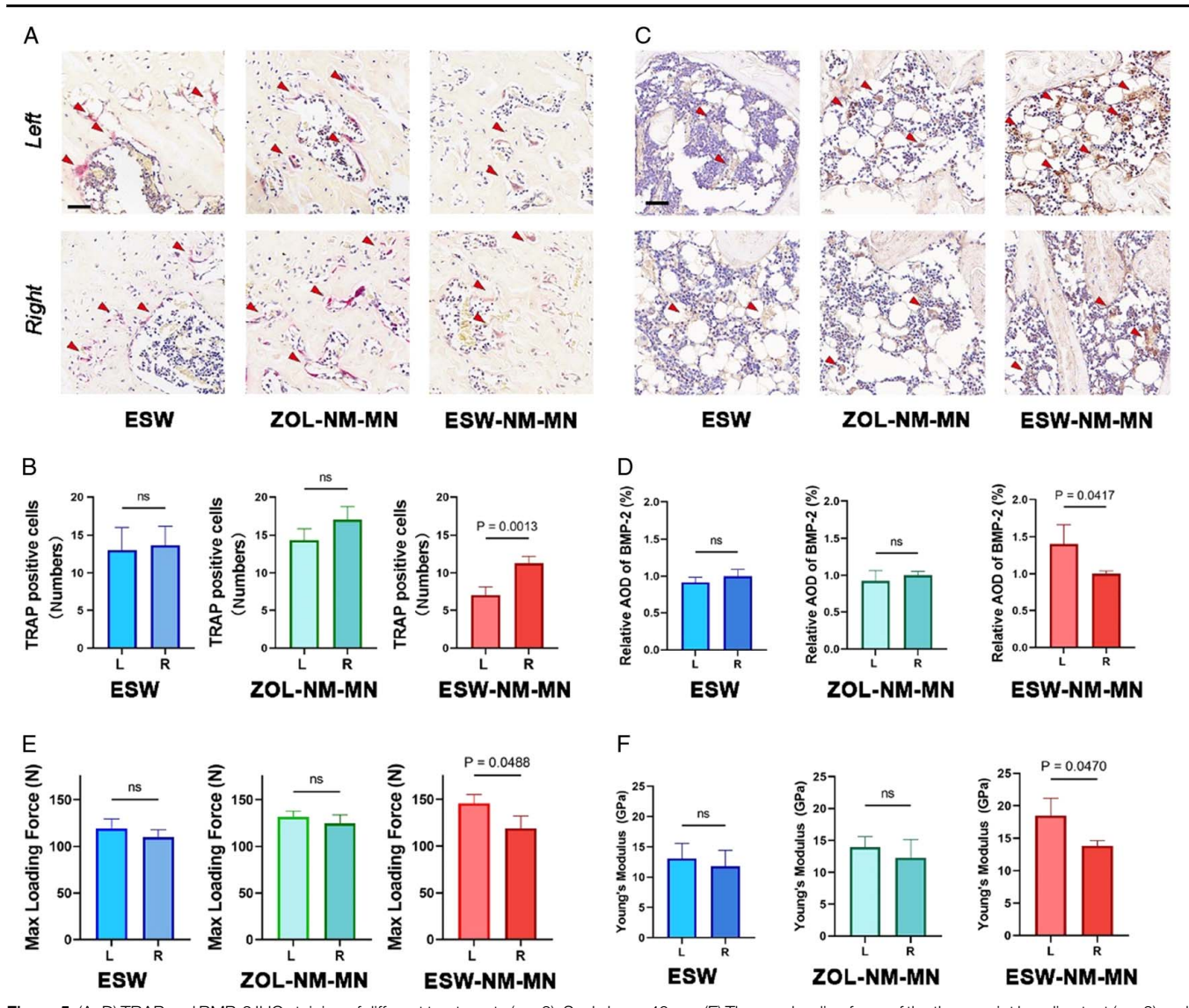


Figure 5. (A–D) TRAP and BMP-2 IHC staining of different treatments (n = 3). Scale bar = 40 μ m. (E) The max loading force of the three-point bending test (n = 3) and (F) the average Young's modulus of femurs in different groups (n = 3).

to that after intravenous administration (Supplementary Fig. S14, Supplemental Digital Content 1, http://links.lww.com/JS9/C143).

The effectiveness of local drug delivery depends on the drugs' ability to penetrate deeply. In our design, the NM must be distinguished from normal tissue in order to absorb ESW energy for movement. The density of NM material decides the substance's absorption behavior of ESW energy. Hence, we selected a hydroxyapatite-like structure for NM according to finite element analysis (Fig. 1A, B). We observed the movement of ZOL-NM by placing it in a 5% gelatin gel and observing it under a dark field microscope. The results showed that the NM moved in a specific direction when subjected to ESW (Fig. 1H), offering the possibility of deep-tissue penetration. With further conjecture, we believe that NMs made with different materials in density could change the depth of penetration, which is used to realize the simultaneous administration of drugs at different depths.

We also verify the vertical motion of ZOL-NM *in vivo*. Once ZOL-NM was applied to the skin, the ZOL-NM remained in the

dermis layer. However, after the application of ESW, a significant amount of ZOL-NM was able to penetrate deeper into the skin (Fig. 2F). The IVIS was used to observe the accumulation of fluorescently labeled ZOL-NM on bone through microneedle delivery. The timing of the ESW application after microneedle treatment was also tested due to the fact that ZOL-NM entering the bloodstream may affect the local distribution. The results showed that the fluorescence intensity of the rat femur increased significantly when ESW was applied immediately after 30 min of microneedle application (Fig. 2H, I), indicating the direct movement of ZOL-NM. No significant changes were observed when ESW was applied after 1, 1.5, and 2 h. These results confirm that ZOL-NM could penetrate into deep tissue like bone, indicating the great value of ESW applications in drug delivery.

As the aging of the population becomes more apparent, the prevention and treatment of osteoporotic fractures are of increasing concern. Mechanical stimulation is a great non-invasive treatment method. Compared with other stimulations such as

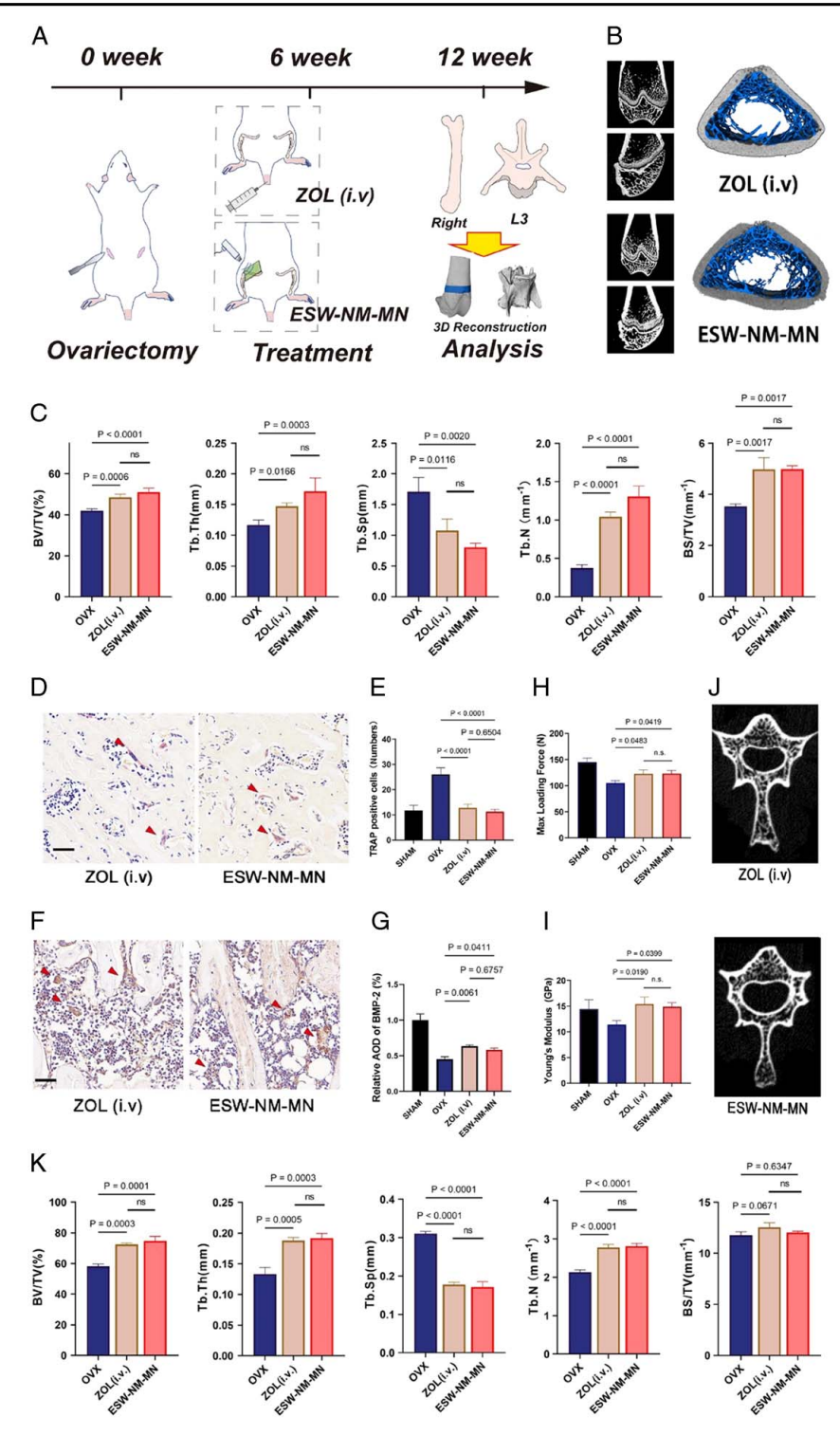


Figure 6. The systemic anti-osteoporosis effects of ZOL-NM *in vivo*. (A, B) The comparison of ZOL (i.v.) and ESW-NM-MN treatments (n = 6). The blue area is in (B) the cancellous bone and the gray area is in (B) the cortical bone. (C) The bone parameters of right femurs in ZOL (i.v.) and ESW-NM-MN treatments (n = 6). (D, E) TRAP staining of ZOL (i.v.) and ESW-NM-MN treatments (n = 3). Scale bar = 40 μ m. (F, G) BMP-2 IHC of ZOL (i.v.) and ESW-NM-MN treatments (n = 3). Scale bar = 40 μ m. (H, I) The max loading force of the three-point bending test and the average Young's modulus of ZOL (i.v.) and ESW-NM-MN treatments (n = 3). (J, K) The CT reconstruction results and statistical analysis of vertebrae (n = 6).

ultrasound, ESW showed higher energy with almost no energy loss in heat during penetration. It can be categorized according to the energy transfer path into focused and radial ESW. The positive and negative phase difference of ESW is greater than that of ultrasound, resulting in generating more pressure, which leads to deep penetration of bone tissue. ESW can stimulate increased differentiation of MSCs into osteoblasts and synthesis and secretion of organic components of bone matrix to form osteoid, followed by mineralization of calcium salt deposits and increased mineralized deposits that mediate neoplastic bone reconstruction^[48,49]. Our experimental results demonstrate the driven force of ESW for deep-tissue penetration, which exerts a significant protective effect on fracture-prone areas and systemic treatment of osteoporosis. Taking advantage of ESW in local deep-tissue drug delivery, we are confident in the application of ESW in other deep-tissue diseases, such as bone tumors. It is worth mentioning that the transdermal delivery system has an advantage in being easy to use, minimally damaging, and has good patient compliance. Still, the enhanced delivery system based on ESW is not yet universal and routine for generalization due to the size of the equipment and there are no miniaturized devices for home use. With further research and development in ESW, we expect to generalize the use of ESW in treating different diseases.

Conclusion

In this paper, our results proved the feasibility of ZOL-NM in deep-tissue disease mediated by ESW. After the soluble MNs delivered the ZOL-NM into the skin, the stiff ZOL-NM was able to penetrate deeply under the cavitation effects of ESW. Besides, the ZOL and Ca²+ could be released from fragmented ZOL-NM to present anti-osteoclastogenesis and pro-osteogenesis. The ZOL-NM in the locality of bone tissue improved bone microarchitecture and the biomechanical properties of bone while exerting systemic therapeutic effects. Hence, the ESW-MN-NM could be treated as a new strategy to prevent fractures by effectively improving local therapeutic effects for deep-tissue disease.

Notes: This work has been reported following the ARRIVE guidelines^[50] (Animals in Research: Reporting In Vivo Experiments), Supplemental Digital Content 4, http://links.lww.com/JS9/C146.

Ethical approval

This study involves animal experiments. Ethical approval for this study (No. IHEPLLSC202005) was provided by the Institutional Animal Ethical Committee of the University of Chinese Academy of Sciences, Beijing, China, in May 2020.

Consent

No human experimentation was involved.

Sources of funding

This work was supported by grants from the National Key Research and Development Program of China (No. 2021YFA1201204), Beijing Nova Program (No. Z211100002121031), National Natural Science Foundation of China (No. 12105312), Guangdong Basic and Applied Basic Research Foundation (2021B1515120037,

2021B1515140042, 2022A1515140037), the Capital Featured Projects (No. Z181100001718018), and the PLA Medical Science and Technology Youth Training Program (No. 17QNP042), and the directional institutionalized scientific research platform relies on Beijing Synchrotron Radiation Facility of Chinese Academy of Sciences.

Author contribution

F.H. and H.L.: methodology, formal analysis, investigation, and writing – original draft; J.X., M.Y., W.H., Y.L., and C.W.: software and validation; H.L., L.L., and Q.L.: methodology, software, validation, visualization, and data curation; J.Z, W.S., and R.C.: methodology, software, and validation; Y.C. and J.L.: software, validation, formal analysis, and supervision; Gengyan X., Gengmei X., and K.C.: conceptualization, writing – review and editing, supervision, project administration, and funding acquisition.

Conflicts of interest disclosure

The authors declare that they have no conflicts of interest.

Guarantor

Gengyan Xing, The Third Medical Center of Chinese People's Liberation Army General Hospital, Beijing 100039, P.R. China; E-mail: xgy1350138@163.com. Gengmei Xing and Kui Chen, Key Laboratory for Biomedical Effects of Nanomaterials and Nanosafety, Institute of High Energy Physics and National Center for Nanosciences and Technology, Chinese Academy of Sciences, Beijing 100043, P.R. China; E-mail: xinggm@ihep.ac.cn; chenkui@ihep.ac.cn.

Data availability statement

Supporting Information is available within the article or from the author.

Acknowledgements

We thank Jinan Laboratory of Applied Nuclear Science, Institute of High Energy Physics, and Chinese Academy of Sciences for providing Micro-CT scanning, and 4W1B and 4B7B experiment stations from Beijing Synchrotron Radiation Facility, Institute of High Energy Physics, Chinese Academy of Sciences for providing Synchrotron Radiation Proportional CT.

References

- [1] Reid IR, Horne AM, Mihov B, et al. Fracture prevention with zoledronate in older women with osteopenia. N Engl J Med 2018;379:2407–16.
- [2] Black DM, Geiger EJ, Eastell R, et al. Atypical femur fracture risk versus fragility fracture prevention with bisphosphonates. N Engl J Med 2020; 383:743–53.
- [3] Black DM, Schwartz AV, Ensrud KE, et al. Effects of continuing or stopping alendronate after 5 years of treatment: the Fracture Intervention Trial Long-term Extension (FLEX): a randomized trial. JAMA 2006;296: 2927–38.
- [4] Gong Y, Bu Y, Li Y, et al. Hydrogel-based delivery system applied in the local anti-osteoporotic bone defects. Front Bioeng Biotechnol 2022;10: 1058300.

- [5] Sabbagh F, Kim BS. Recent advances in polymeric transdermal drug delivery systems. J Control Release 2022;341:132–46.
- [6] Yang G, Chen Q, Wen D, et al. A therapeutic microneedle patch made from hair-derived keratin for promoting hair regrowth. ACS Nano 2019; 13:4354–60.
- [7] Ye Y, Wang J, Hu Q, et al. Synergistic transcutaneous immunotherapy enhances antitumor immune responses through delivery of checkpoint inhibitors. ACS Nano 2016;10:8956–63.
- [8] Chen Z, Li H, Bian Y, et al. Bioorthogonal catalytic patch. Nat Nanotechnol 2021;16:933–41.
- [9] Prausnitz MR, Langer R. Transdermal drug delivery. Nat Biotechnol 2008;26:1261–8.
- [10] Prausnitz MR. Microneedles for transdermal drug delivery. Adv Drug Deliv Rev 2004;56:581–7.
- [11] DeMuth PC, Min Y, Huang B, et al. Polymer multilayer tattooing for enhanced DNA vaccination. Nat Mater 2013;12:367–76.
- [12] Yu J, Zhang Y, Ye Y, et al. Microneedle-array patches loaded with hypoxia-sensitive vesicles provide fast glucose-responsive insulin delivery. Proc Natl Acad Sci U S A 2015;112:8260–5.
- [13] Chang H, Chew SWT, Zheng M, *et al.* Cryomicroneedles for transdermal cell delivery. Nat Biomed Eng 2021;5:1008–18.
- [14] Lopez-Ramirez MA, Soto F, Wang C, et al. Built-in active microneedle patch with enhanced autonomous drug delivery. Adv Mater 2020;32:1905740.
- [15] Kováčik A, Kopečná M, Vávrová K. Permeation enhancers in transdermal drug delivery: benefits and limitations. Expert Opin Drug Deliv 2020; 17:145–55.
- [16] Liu A, Wang Q, Zhao Z, et al. Nitric oxide nanomotor driving exosomesloaded microneedles for achilles tendinopathy healing. ACS Nano 2021; 15:13339–50.
- [17] Qin Y, Geng X, Sun Y, et al. Ultrasound nanotheranostics: toward precision medicine. J Control Release 2023;353:105–24.
- [18] Ligrani PM, McNabb ES, Collopy H, et al. Recent investigations of shock wave effects and interactions. Adv Aerodyn 2020;2:4.
- [19] Liang H, Chen K, Xie J, et al. A bone-penetrating precise controllable drug release system enables localized treatment of osteoporotic fracture prevention via modulating osteoblast–osteoclast communication. Small 2023;19:e2207195.
- [20] Liang W, Chen K, Lv L, et al. Radial extracorporeal shock wave responsive precise nanoplatform for effective osteoporosis sequential treatment. Chem Eng J 2021;425:130687.
- [21] Brotchie A, Mettin R, Grieser F, et al. Cavitation activation by dual-frequency ultrasound and shock waves. Phys Chem Chem Phys 2009;11: 10029–34.
- [22] Huang D, Wang J, Song C, et al. Ultrasound-responsive matters for biomedical applications. Innovation (Camb) 2023;4:100421.
- [23] He W, Tao J, Pan H, et al. A size-controlled synthesis of hollow apatite nanospheres at water-oil interfaces. Chem Lett 2010;39:674–5.
- [24] Chen K, Wang Y, Liang H, *et al.* Fullerenols boosting the therapeutic effect of anti-CD47 antibody to trigger robust anti-tumor immunity by inducing calreticulin exposure. Nano Today 2021;37:101070.
- [25] Geng H, Chang YN, Bai X, et al. Fullerenol nanoparticles suppress RANKL-induced osteoclastogenesis by inhibiting differentiation and maturation. Nanoscale 2017;9:12516–23.
- [26] Chen K, Zhou R, Liang H, et al. Reversing the pathological microenvironment by radiocatalytic sensitizer for local orthotopic osteosarcoma radiotherapy enhancement. Nano Today 2023;48:101739.
- [27] Chen K, Geng H, Liang W, et al. Modulated podosome patterning in osteoclasts by fullerenol nanoparticles disturbs the bone resorption for osteoporosis treatment. Nanoscale 2020;12:9359–65.
- [28] Gu W, Chen K, Zhao X, et al. Highly dispersed fullerenols hamper osteoclast ruffled border formation by perturbing Ca²⁺ bundles. Small 2018;14:1802549.

- [29] Deckard C, Walker A, Hill BJ. Using three-point bending to evaluate tibia bone strength in ovariectomized young mice. J Biol Phys 2017;43: 139–48.
- [30] Wang C, Sun CC. A critical examination of three-point bending for determining Young's modulus. Int J Pharm 2022;629:122409.
- [31] Zhang Z, Yan H, Cao W, et al. Ultrasound-chargeable persistent luminescence nanoparticles to generate self-propelled motion and photothermal/NO therapy for synergistic tumor treatment. ACS Nano 2023;17:16089–106.
- [32] Zheng J, Wang W, Gao X, et al. Cascade catalytically released nitric oxide-driven nanomotor with enhanced penetration for antibiofilm. Small 2022;18:2205252.
- [33] Shao J, Cao S, Williams DS, et al. Photoactivated polymersome nanomotors: traversing biological barriers. Angew Chem Int Ed 2020;59: 16918–25.
- [34] Luo S, Yang G, Chen J, et al. In-situ studies and simulation of equiaxed solidification in Al–20Cu alloy. Mater Sci Technol 2021;37:59–65.
- [35] Rahmani P, Morin S. Prevention of osteoporosis-related fractures among postmenopausal women and older men. CMAJ 2009;181:815–20.
- [36] Tanaka T, Takao-Kawabata R, Takakura A, et al. Teriparatide relieves ovariectomy-induced hyperalgesia in rats, suggesting the involvement of functional regulation in primary sensory neurons by PTH-mediated signaling. Sci Rep 2020;10:5346.
- [37] Liu J, Xiao Q, Xiao J, et al. Wnt/beta-catenin signalling: function, biological mechanisms, and therapeutic opportunities. Signal Transduct Target Ther 2022;7:3.
- [38] Chen T, Wang Y, Hao Z, et al. Parathyroid hormone and its related peptides in bone metabolism. Biochem Pharmacol 2021;192:114669.
- [39] Bolognese MA. SERMs and SERMs with estrogen for postmenopausal osteoporosis. Rev Endocr Metab Disord 2010;11:253–9.
- [40] Austin LA, Heath H3rd. Calcitonin: physiology and pathophysiology. N Engl J Med 1981;304:269–78.
- [41] Drake MT, Clarke BL, Khosla S. Bisphosphonates: mechanism of action and role in clinical practice. Mayo Clin Proc 2008;83:1032–45.
- [42] Gizzo S, Saccardi C, Patrelli TS, et al. Update on raloxifene: mechanism of action, clinical efficacy, adverse effects, and contraindications. Obstet Gynecol Surv 2013;68:467–81.
- [43] Yu P, Liu Y, Xie J, et al. Spatiotemporally controlled calcitonin delivery: long-term and targeted therapy of skeletal diseases. J Control Release 2021;338:486–504.
- [44] Hsiao CY, Chen TH, Chu TH, et al. Calcitonin induces bone formation by increasing expression of Wnt10b in osteoclasts in ovariectomy-induced osteoporotic rats. Front Endocrinol (Lausanne) 2020;11:613.
- [45] Wang B, Zhan Y, Yan L, et al. How zoledronic acid improves osteoporosis by acting on osteoclasts. Front Pharmacol 2022;13: 961941.
- [46] Chen T, Berenson J, Vescio R, et al. Pharmacokinetics and pharmacodynamics of zoledronic acid in cancer patients with bone metastases. J Clin Pharmacol 2002;42:1228–36.
- [47] Pazianas M. Atorvastatin reduces zoledronic acid-induced osteonecrosis of the jaws of rats. Bone 2022;165:116561.
- [48] Chen Y, Xu J, Huang Z, et al. An innovative approach for enhancing bone defect healing using PLGA scaffolds seeded with extracorporealshock-wave-treated bone marrow mesenchymal stem cells (BMSCs). Sci Rep 2017;7:44130.
- [49] Schaden W, Mittermayr R, Haffner N, et al. Extracorporeal shockwave therapy (ESWT)--first choice treatment of fracture non-unions? Int J Surg 2015;24(Pt B):179–83.
- [50] Kilkenny C, Browne WJ, Cuthill IC, et al. Improving bioscience research reporting: the ARRIVE guidelines for rep orting animal research. PLoS Biol 2010;8:e1000412.